

Magnon Condensation in Dimerized Antiferromagnets with Spin-Orbit Coupling

Qi-Rong Zhao,¹ Meng-Jie Sun,¹ Zheng-Xin Liu,^{1,2,*} and Jiucui Wang^{3,1,†}

¹Department of Physics, Renmin University of China, Beijing 100872, China

²Tsung-Dao Lee Institute & School of Physics and Astronomy,
Shanghai Jiao Tong University, Shanghai 200240, China

³Institute for Advanced Study, Tsinghua University, Beijing 100084, China

(Dated: April 20, 2022)

Bose-Einstein condensation (BEC) of triplet excitations triggered by a magnetic field, sometimes called antiferromagnon BEC, in dimerized antiferromagnets gives rise to a long-range antiferromagnetic order in the plane perpendicular to the applied magnetic field. To explore the effects of spin-orbit coupling on magnon condensation, we study the spin model on the distorted honeycomb lattice with dimerized Heisenberg exchange (J terms) and uniform off-diagonal exchange (Γ' terms) interactions. By using variational Monte Carlo method and spin wave theory, we find that an out-of-plane magnetic field can induce different types of long-range magnetic orders, no matter if the ground state is a non-magnetic dimerized state or an antiferromagnetically ordered Néel state. Furthermore, the critical properties of field-driven phase transitions in systems with spin-orbit coupling can be different from the conventional magnon BEC. Our study is helpful to understand the rich phases of spin-orbit coupled antiferromagnets in an external magnetic field.

I. INTRODUCTION

Quantum magnetism, which involves interacting spins and orbitals in magnetic materials, is a good platform to investigate many-body physics. The quantum dimer magnet (QDM), a nonmagnetic ground state constituted by distinct singlet-dimers, is one of the simplest examples of quantum magnets having no classical correspondence. An example of QDMs is the antiferromagnetic (AFM) Heisenberg model on the distorted honeycomb lattice, where the shorter bonds (e.g. the vertical bonds, see Fig.1 for illustration) form disconnected dimers. Since the interactions on the longer bonds are relatively weaker, the ground state can be approximately considered as a direct product of singlets formed by the dimers. The excitation on each singlet dimer forms a triplet, which is bosonic and sometimes called a ‘magnon’.

It was proposed that the ‘magnons’ in the QDMs can undergo BEC¹ just like usual Bose gas². An external magnetic field can adjust the ‘chemical potential’ of the magnons, consequently a magnon-BEC phase appears at the intermediate field region which is sandwiched by the dimerized phase at the low-field side and polarized phase at the high-field side. The magnon BEC was experimentally verified later^{3–12}. As is known that the BEC of usual bosons spontaneously breaks the particle number conserving global $U(1)$ symmetry, similarly the BEC of magnons spontaneously breaks the $O(2)$ spin rotational symmetry^{13,14}. Here the $O(2)$ group consists of continuous spin rotation along the direction of the magnetic field $\mathbf{B} \parallel \hat{z}$ which preserves the spin angular momentum S^z . The spontaneous breaking of $O(2)$ symmetry indicates the appearance of long-range antiferromagnetic order in the plane perpendicular to the field direction. However, unlike the coherent global phase of the BEC in repulsively interacting bosons which can cause interference, the global phase of the magnon BEC corresponds to the orientation of the magnetic momenta and has

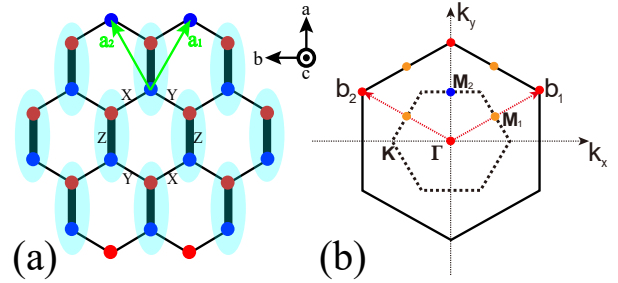


FIG. 1: (a) An illustration of the dimerized honeycomb lattice structure. The thickness of bonds indicates the strength of Heisenberg (J) interactions, and the x , y , and z bonds in J - Γ' model are shown. The crystallographic a (in-plane), b (in-plane), and c (out-of-plane) directions are indicated, whose directions are given by $[1\bar{1}0]$, $[11\bar{2}]$, and $[111]$, respectively. (b) The corresponding Brillouin zone of honeycomb lattice spanned by unit vectors \bar{a}_1 and \bar{a}_2 .

no interference effect.

Generally, in the real magnetic materials, the continuous $O(2)$ symmetry explicitly breaks down to its discrete subgroups if the system contains anisotropic interactions, such as dipole-dipole interactions or spin-orbit coupling (SOC)¹⁵. If the anisotropy of the spin-spin interactions is strong enough, the physical consequences of the applied magnetic field will be modified. For instance, in an external magnetic field, the dimer compound $\text{Yb}_2\text{Si}_2\text{O}_7$ ¹⁶ contains two intermediate phases between the dimerized phase and the polarized phase, which is beyond the usual magnon BEC mechanism. A previous theoretical work attributes the existence of two nontrivial intermediate phases to the anisotropy in the exchange interactions and the staggered Landé g factor¹⁷. Alternatively, SOC is also a possible reason which yields the new phases in the intermediate field region.

If the energy scale of the physical origin (e.g. the

SOC) that causes the anisotropy in the interactions and explicitly breaks the continuous $O(2)$ symmetry is very weak compared to the ordering temperature, the low energy physics is approximately described by S^z conserving theory^{18–20}. Therefore, it is expected that the physical picture of magnon BEC still works under an external magnetic field. But it is unclear what would happen if SOC becomes strong. In the rest part of this work, we shall illustrate that although the continuous symmetry is no longer a good approximation, *the magnetic-field-induced long-range AFM orders are quite general in dimerized antiferromagnets with SOC*. The magnetic order in the intermediate field region can be either Néel order, or stripe order, or zigzag order, depending on the details of interactions. Even when the ground state is Néel ordered state under zero field (owing to strong SOC), the stripe order or the zigzag order can still emerge in the intermediate field region.

We will begin with an antiferromagnetic spin model on the honeycomb lattice with finite SOC. The interactions include the Heisenberg J terms and the off-diagonal Γ' terms, namely,

$$H = \sum_{\langle i,j \rangle \in \gamma} J_\gamma \mathbf{S}_i \cdot \mathbf{S}_j + \Gamma' \left(S_i^\alpha S_j^\gamma + S_i^\gamma S_j^\alpha + S_i^\beta S_j^\gamma + S_i^\gamma S_j^\beta \right) - g\mu_B \sum_i \mathbf{B} \cdot \mathbf{S}_i, \quad (1)$$

where $\langle i, j \rangle$ denotes nearest-neighbor sites, $\alpha, \beta, \gamma = x, y, z$ stand the spin indices, and $\gamma = x, y, z$ is also used to label the three types of bonds (see Fig.1 for illustration). We adopt the setting with $J_x = J_y \leq J_z$ and $g\mu_B = 1$. With variational Monte Carlo (VMC) calculations using Gutzwiller projected states as trial wave functions, we found that, in addition to the field-induced Néel order, the zigzag order and the stripe order can also appear in the intermediate magnetic fields (see Fig.2 for the phase diagram). This suggests that SOC caused frustration is crucial to understand the nature of the field-induced quantum critical points and the magnetic orders in the intermediate field region (see Ref. 21, 22 for another example of model study).

The rest part of the paper is organized as follows. In Sec.II, we introduce the symmetry group of the extended Heisenberg model (the J - Γ' model) on the honeycomb lattice. In Sec.III, we present the technical details of the VMC method, especially for the ground state and excited states. Readers who are not interested in the details of the method can skip Sec.III and go to Sec.IV directly, where the VMC results are presented. Sec.V is devoted to the bosonic effective theory aiming to interpret the origin of the intermediate magnetically ordered phases and the nature of quantum critical points. Finally, the paper is concluded in Sec.VI.

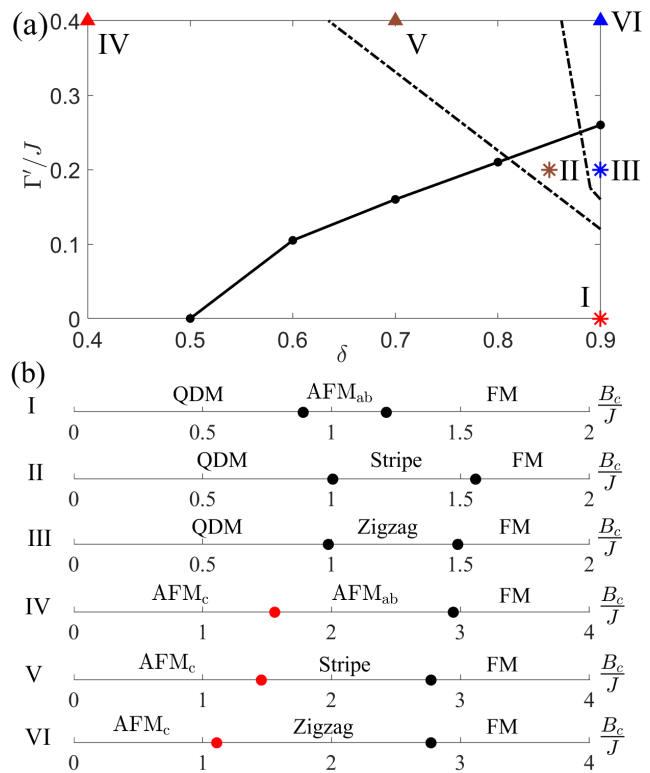


FIG. 2: (a) The zero-field quantum phase diagram contains two phases, the QDM phase (lower) and the AFM_c phase (upper), separated by a continuous transition (illustrated by the solid line). In AFM_c phase, the magnetic momentum is parallel to the c -direction. With increasing of field strength, different magnetic orders (including AFM_{ab}, stripe, and zigzag) appear at the intermediate field region, accordingly the QDM phase splits into three different pieces labeled with I, II, III. (b)(I)~(III), corresponding to the three stellate points in I~III respectively, show the phase transitions with the increasing of field strength along c -direction. The AFM_c phase also splits into three different regions according to the magnetic orders emerging at intermediate field strength, labeled with IV, V, VI. The phase transition diagrams with the increasing B_c for the three triangular points in IV~VI are shown in (b)(IV)~(VI), respectively. The red (black) solid points represent first-order (continuous) phase transitions.

II. SYMMETRY GROUP OF THE SPIN MODEL

Generally, SOC in quantum magnets locks the spin rotation operations with the corresponding lattice rotations and hence reduce the continuous spin rotation symmetries to discrete ones. A class of spin-orbit coupled antiferromagnets on the honeycomb lattice has the discrete symmetry group D_{3d} ^{23–27} and contains anisotropic spin-spin interactions in addition to the isotropic Heisenberg exchanges (J terms). The anisotropic interactions include, the diagonal Kitaev type exchange terms $S_i^\gamma S_j^\gamma$ (K terms)^{28–30} and the off-diagonal exchange interactions such as the $S_i^\alpha S_j^\beta + S_i^\beta S_j^\alpha$ interactions (Γ terms)^{31,32}

or the $S_i^\alpha S_j^\gamma + S_i^\gamma S_j^\alpha + S_i^\beta S_j^\gamma + S_i^\gamma S_j^\beta$ interactions (Γ' terms)^{33–36}, here $\alpha, \beta, \gamma = x, y, z$ and we have only listed the interactions on the γ -bond.

On the other hand, some honeycomb-lattice materials are dimerized where the threefold rotational symmetry is absent. Supposing that the z -bonds are shorter than the other bonds, then it is expected that the strength of interactions is stronger on the z -bonds (see Fig.1). In the present work, we will focus on the simple model (1) on dimerized honeycomb lattice containing J and Γ' interactions only. Here we adopt the Γ' term but do not consider other terms because the Γ' interactions can give rise to a richer magnetic structure. For simplicity, we assume that the strength of Γ' interactions are equal on all the bonds, while the strength of the Heisenberg terms is anisotropic. Thus we introduce a parameter δ to denote the relative difference of J between the z -bonds and the x, y -bonds, with $J_z = J = 1$ and $J_x = J_y = (1 - \delta)J$, $\delta \in [0, 1]$. The magnetic field is applied along the c -direction with $\mathbf{B} = B_c(1, 1, 1)/\sqrt{3}$.

If $\delta = 0, \mathbf{B} = 0$, the system has $D_{3d} \times Z_2^T$ symmetry³⁷, where Z_2^T stands for the time reversal symmetry. If $\delta \neq 0, \mathbf{B} = 0$, the system has $\{E, P, C_2, M\} \times Z_2^T$ magnetic point-group symmetry³⁸, with P the spatial inversion, C_2 the twofold rotation along the z -bond, and $M = C_2P$ the mirror reflection symmetry. For general values of δ and \mathbf{B} (e.g. $\delta \neq 0, \mathbf{B} \neq 0$), the symmetry of the model reduces to the following magnetic point group $2'/m' = \{E, P, C_2T, MT\}$, with T the time reversal.

In the following, we will study the phase diagram and the nature of the phases for the model (1) using VMC approach.

III. THE VMC APPROACH

A. For the Ground States

The VMC approach is based on spinon representation, where the spin operators are written in quadratic forms of fermionic spinons $S_i^m = \frac{1}{2}C_i^\dagger \sigma^m C_i$, where $C_i^\dagger = (c_{i\uparrow}^\dagger, c_{i\downarrow}^\dagger)$, $m \equiv x, y, z$, and σ^m are Pauli matrices. The particle number constraint, $\hat{N}_i = c_{i\uparrow}^\dagger c_{i\uparrow} + c_{i\downarrow}^\dagger c_{i\downarrow} = 1$, should be imposed at every site such that the size of the Hilbert space of the fermions is the same as that of the original spin. It is convenient to introduce the matrix operator $\psi_i = (C_i, \bar{C}_i)$ with $\bar{C}_i = (c_{i\downarrow}^\dagger, -c_{i\uparrow}^\dagger)^T$ such that the spin operators can also be written as $S_i^m = \text{Tr}(\psi_i^\dagger \frac{\sigma^m}{4} \psi_i)$. Since the spin operator is invariant under a local $SU(2)$ transformation $\psi_i \rightarrow \psi_i W_i$, the fermionic spinon representation has an $SU(2)$ gauge symmetry³⁹.

The spin interactions are rewritten in terms of interacting fermionic operators and are further decoupled into a non-interacting mean-field Hamiltonian. Then we perform Gutzwiller projection to the mean-field ground state $|\Psi_{\text{mf}}(\mathbf{R})\rangle$ to enforce the particle number constraint. The projected states $|\Psi(\mathbf{R})\rangle = P_G |\Psi_{\text{mf}}(\mathbf{R})\rangle$ provide a

series of trial wave functions depending on the choice of the mean-field Hamiltonian $H_{\text{mf}}(\mathbf{R})$, where P_G denotes a Gutzwiller projection and \mathbf{R} are treated as variational parameters. The energy of the trial state $E(\mathbf{R}) = \langle \Psi(\mathbf{R}) | H | \Psi(\mathbf{R}) \rangle / \langle \Psi(\mathbf{R}) | \Psi(\mathbf{R}) \rangle$ is computed using Monte Carlo sampling, and the optimal parameters \mathbf{R} are determined by minimizing the energy $E(\mathbf{R})$. In the following, we will focus on the construction of the trial mean-field Hamiltonian.

The Heisenberg interactions can be decoupled into a non-interacting fermionic Hamiltonian,

$$H_{\text{mf}}^J = \sum_{\langle i, j \rangle \in \gamma} \left(t^\gamma C_i^\dagger C_j + \Delta^\gamma C_i^\dagger \bar{C}_j + \text{H.c.} \right) + \sum_i \text{Tr} \left(\lambda_i \cdot \psi_i \tau \psi_i^\dagger \right) \quad (2)$$

where t^γ denotes singlet hopping and Δ^γ represents singlet pairing. $\lambda^{x, y, z}$ are three Lagrangian multipliers to ensure the $SU(2)$ gauge invariance (where the λ^z component corresponds to the particle number constraint).

To decouple the Γ' interactions, we adopt the mean-field Hamiltonian appeared in literature^{37,38,40}, namely,

$$H_{\text{mf}}^{\Gamma'} = \sum_{\langle i, j \rangle \in \gamma} i\rho_c \text{Tr} \left(\psi_i^\dagger \psi_j + \tau^x \psi_i^\dagger \sigma^x \psi_j + \tau^y \psi_i^\dagger \sigma^y \psi_j + \tau^z \psi_i^\dagger \sigma^z \psi_j \right) + i\rho_b \text{Tr} \left(\tau^\alpha \psi_i^\dagger \sigma^\gamma \psi_j + \tau^\gamma \psi_i^\dagger \sigma^\alpha \psi_j + \tau^\beta \psi_i^\dagger \sigma^\gamma \psi_j + \tau^\gamma \psi_i^\dagger \sigma^\beta \psi_j \right) + \text{H.c.} \quad (3)$$

where ρ_b and ρ_c are both real numbers.

The Zeeman coupling is simply written as

$$H^B = - \sum_i \text{Tr} \left(\mathbf{B} \cdot \psi_i^\dagger \frac{\boldsymbol{\sigma}}{2} \psi_i \right). \quad (4)$$

Finally, to describe the field-induced magnetic order in the J - Γ' model, we introduce a background field \mathbf{M}_i to induce the symmetry-breaking magnetic order. The ordering pattern \mathbf{M}_i is assumed to contain a single momentum \mathbf{Q} with⁴¹

$$\mathbf{M}_i = M \{ \sin \phi [\hat{\mathbf{e}}_x \cos(\mathbf{Q} \cdot \mathbf{r}_i) + \hat{\mathbf{e}}_y \sin(\mathbf{Q} \cdot \mathbf{r}_i)] + \cos \phi \hat{\mathbf{e}}_z \},$$

where \mathbf{Q} is the ordering momentum, $\hat{\mathbf{e}}_{x, y, z}$ are the local spin axes, and ϕ is the canting angle. The ordering momentum \mathbf{Q} is adopted either from the classical ground state or the classical metastable states (the \mathbf{Q} from the classical ground state is not always the one with the lowest energy after quantum corrections are considered). For a given \mathbf{Q} , the local axes $\hat{\mathbf{e}}_{x, y, z}$ are fixed as they are in the classical state, while M and ϕ are treated as variational parameters.

Hence the complete trial mean-field Hamiltonian (with nearest-neighbor coupling terms only) for the J - Γ' model in an external magnetic field reads

$$H_{\text{mf}}^{\text{total}} = H_{\text{mf}}^J + H_{\text{mf}}^{\Gamma'} + H^B - \frac{1}{2} \sum_i (\mathbf{M}_i \cdot C_i^\dagger \boldsymbol{\sigma} C_i + \text{H.c.}). \quad (5)$$

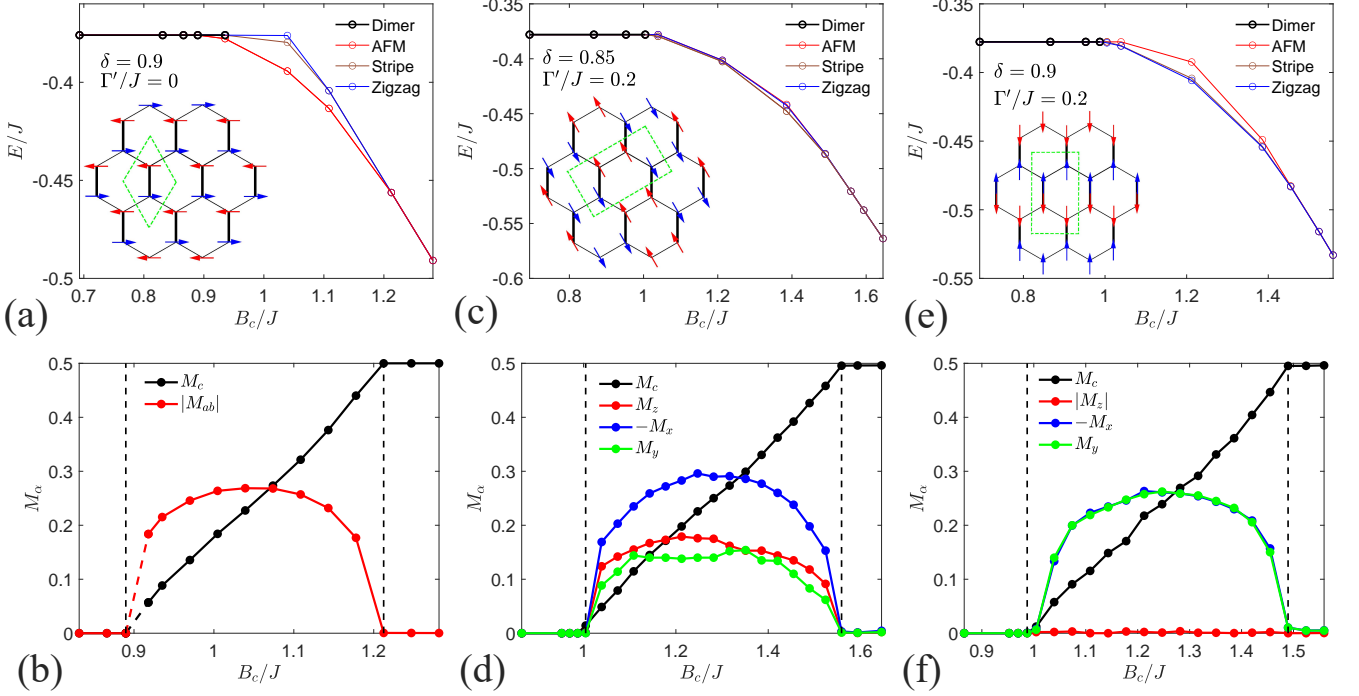


FIG. 3: Energy curves (the upper figures) and magnetization of ground states (the lower figures) with increasing magnetic field for (a)&(b) $\delta=0.9$, $\Gamma'/J=0$, (c)&(d) $\delta=0.85$, $\Gamma'/J=0.2$, (e)&(f) $\delta=0.9$, $\Gamma'/J=0.2$. The insets of (a), (c), (e) show the spin configurations of Néel, stripe, and zigzag orders, respectively. The vertical dashed lines indicate the values of the critical fields.

The complete set of variational parameters include $(t^\gamma, \Delta^\gamma, \rho_b, \rho_c, \lambda, M, \phi)$ whose optimal values are determined by minimizing the energy of the Gutzwiller projected wave function.

In the variational process, we firstly choose a classical metastable configuration with \mathbf{Q} , then optimize the energy of the projected state. By comparing the optimal energies of different trial \mathbf{Q} s, we obtain the approximate ground state.

In addition to determining the phase diagram (see Fig.2 and Fig.3), the VMC method can further provide information on the low-energy excitations.

B. For the Spinons Excited States

Now we try to construct the low-energy excitations via Gutzwiller projected spinons excited states

$$|\mathbf{k}; (\mathbf{k}-\mathbf{q})_m, (\mathbf{q})_n\rangle = P_G f_{\mathbf{k}-\mathbf{q},m}^\dagger f_{\mathbf{q},n}^\dagger |\Psi_{\text{mf}}\rangle, \quad (6)$$

where $f_{\mathbf{k}-\mathbf{q},m}$ and $f_{\mathbf{q},n}$ are eigen particles of the mean-field Hamiltonian, with m, n the band indices and \mathbf{k}, \mathbf{q} the lattice momentum according to the translation operators.

The above two-spinon excitations form a continuum and do not correctly describe the low-energy excitations of the system. The failure of the state (6) in describing the low-energy excitations is owing to the strong gauge interactions between the spinons which are not correctly

addressed. To partially solve this problem, we diagonalize the original Hamiltonian in the subspace spanned by the two-spinon excitation continuum⁴²⁻⁴⁵. Specifically, we calculate the matrix elements of the matrix $\mathcal{H}(\mathbf{k})$ with

$$\mathcal{H}_{p_m n, q_m' n'}(\mathbf{k}) = \langle \mathbf{k}; (\mathbf{k}-\mathbf{p})_m, (\mathbf{p})_n | H | \mathbf{k}; (\mathbf{k}-\mathbf{q})_{m'}, (\mathbf{q})_{n'} \rangle,$$

where \mathbf{k} is the total momentum of the state with a pair of spinons excitation. The dimensionality $(2N \times C)$ of this matrix $\mathcal{H}(\mathbf{k})$ is equal to twice the total number of sites N times the size of the unit cell C in the corresponding mean-field Hamiltonian.

Since the states in the two-spinon continuum are not orthogonal, we need to calculate the metric matrix g formed by the overlap of the states,

$$g_{p_m n, q_m' n'}(\mathbf{k}) = \langle \mathbf{k}; (\mathbf{k}-\mathbf{p})_m, (\mathbf{p})_n | \mathbf{k}; (\mathbf{k}-\mathbf{q})_{m'}, (\mathbf{q})_{n'} \rangle.$$

Hence, the eigenproblem of $\mathcal{H}(\mathbf{k})$ should be calculated by

$$g^{-1}(\mathbf{k}) \mathcal{H}(\mathbf{k}) U = U \cdot \text{diag}(\epsilon_1, \dots, \epsilon_{2CN}),$$

where the eigenvalues $\epsilon_1, \dots, \epsilon_{2CN}$ are the ‘renormalized’ energy of the excitations.

The renormalized eigenfunction $|\mathbf{k}\rangle_{\text{rn}}$ is given by

$$|\mathbf{k}\rangle_{\text{rn}} = \sum_{\mathbf{q} \in \text{BZ}} \mathcal{F}(qmn) |\mathbf{k}; (\mathbf{k}-\mathbf{q})_m, (\mathbf{q})_n\rangle,$$

where $\mathcal{F}(qmn)$ is the eigenvector of the matrix \mathcal{H} .

It will be shown that in the magnetically ordered phase the two-spin excitations are strongly renormalized and the bound state formed by the spinons pair behaves like a magnon (see Fig.4 and Fig.5).

IV. THE VMC RESULTS

A. The Phase Diagram

Our VMC calculations are performed on a tori of 6×6 unit cells, *i.e.* of 72 lattice sites. The result is shown in Fig.2. The (Γ', δ) -parameter space is divided into several different regions. Firstly, when $\mathbf{B} = 0$, the phase diagram contains two phases which are separated by the solid line. The lower one is a QDM phase, while the upper one is a Néel ordered state locating perpendicular to the honeycomb plane (namely, AFM_c). The phase transition is of second order with dynamical critical exponent $z = 1$ (see Appendix A1 for details) which is characterized by the spontaneous breaking of spatial inversion symmetry.

When $B \neq 0$, according to the pattern of intermediate magnetic orders at intermediate magnetic fields, each phase is divided into three different regions.

In region-I, the Γ' interaction is relatively small, the SOC is not strong enough to change the physics of magnon BEC. Namely, there is an intermediate canted AFM with long-range magnetic order with Néel pattern in the plane perpendicular to the field (namely, AFM_{ab}) between the low-field QDM phase and the high-field polarized phase [see Fig.3(a) for illustration], just as the case $\Gamma' = 0$. The magnon excitations are gapless in the intermediate AFM_{ab} phase although $\Gamma' \neq 0$. It can also be seen that either the canted stripe order or canted zigzag order with long-range magnetic order in the plane perpendicular to the field (namely, stripe or zigzag) is competing in energy with the Néel state. With the increasing of field strength, the phase transitions into the AFM_{ab} phase and out of AFM_{ab} phase are both of second order, which is the same as the case with $\Gamma' = 0$. Here we clarify the fact that the magnetization of the ground state has a small jump at the low-field transition point which seems to indicate a weakly first-order transition. We speculate that this is an artifact owing to the VMC method, where the magnetic order is induced by a static background field. We could resolve the problem through 'renormalization' in VMC framework that allows the ground state to include more spin-wave fluctuations, which will smoothen the magnetization curve. Meanwhile, the nature of the phase transitions will be analyzed in the next section using the renormalized spinons excitations.

With the increasing of Γ' and δ , the region-II shows up. The difference is that in the intermediate phase the stripe ordered state is slightly lower in energy than the Néel state and the zigzag state [see Fig.3(c) for illustration]. In the stripe ordered phase, the spin components

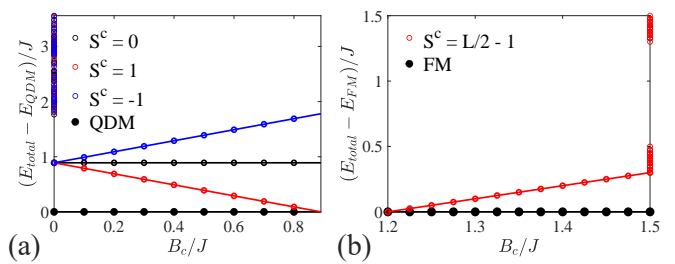


FIG. 4: Energy spectrum at Γ point ($\mathbf{k} = 0$) as a function of magnetic field strength, where the interaction parameters are fixed as $J = 1, \delta = 0.9, \Gamma' = 0$. (a) VMC is used in the QDM phase. At $B_c = 0$, the system has a spin-singlet ground state, gapped triplet excitations (with $S^c = 0, \pm 1$) owing to the continuous $SU(2)$ spin rotational symmetry and higher-energy continuum spectra. All these states are unaffected by the field below $|B_c/J| < 0.89$ but the energy changes linearly with B_c until the gap closes. (b) Exact diagonalization in the polarized limit. As $B_c/J \geq 1.2$, the ground state is fully polarized with $S^c = L/2$, while the excited states with $S^c = L/2 - 1$ form a continuum with a gap above the ground state. These states are unaffected by the field but the energy changes linearly with B_c until the gap closes at $B_c/J = 1.2$.

in the honeycomb plane are pointing along $[\bar{2}11]$ direction (see Fig.3(d)), although the canting direction is slightly away from c-direction. Among the symmetry elements $2'/m' = \{E, P, C_2T, MT\}$ of the Hamiltonian, the C_2T and MT symmetries are broken by the stripe order. The magnon excitations of the stripe phase are gapped, which is different from the case in AFM_{ab} state. Our numerical simulations strongly suggest that the transition between the intermediate stripe state and the dimerized (or polarized) state is continuous, which is in agreement with its spontaneous symmetry breaking.

With further increasing of δ , the system enters the region-III, where the intermediate phase exhibits zigzag type magnetic order (see Fig.3(e) for illustration). The in-plane zigzag order is orienting along the $[1\bar{1}0]$ direction (see Fig.3(f)), which breaks the C_2T symmetry but preserves the MT symmetry. The magnon excitations of the zigzag phase are also gapped. The phase transition between the intermediate zigzag state and the dimerized (or polarized) state is also continuous owing to spontaneous symmetry breaking, which is the same as the case in region-II.

In the left up region, owing to the relatively large Γ' , the ground state at $\mathbf{B} = 0$ is no longer the QDM state with singlet dimers but is replaced by an AFM_c state. Among the symmetry elements $2'/m' = \{E, P, C_2T, MT\}$ of the Hamiltonian, the MT and P symmetries are broken by the AFM_c order at low fields. According to the response to the magnetic field, this region is further divided into three parts. In the first part, with the increase of magnetic field, there is an intermediate AFM ordered state (with Néel pattern in the honeycomb plane, called AFM_{ab}) under a proper mag-

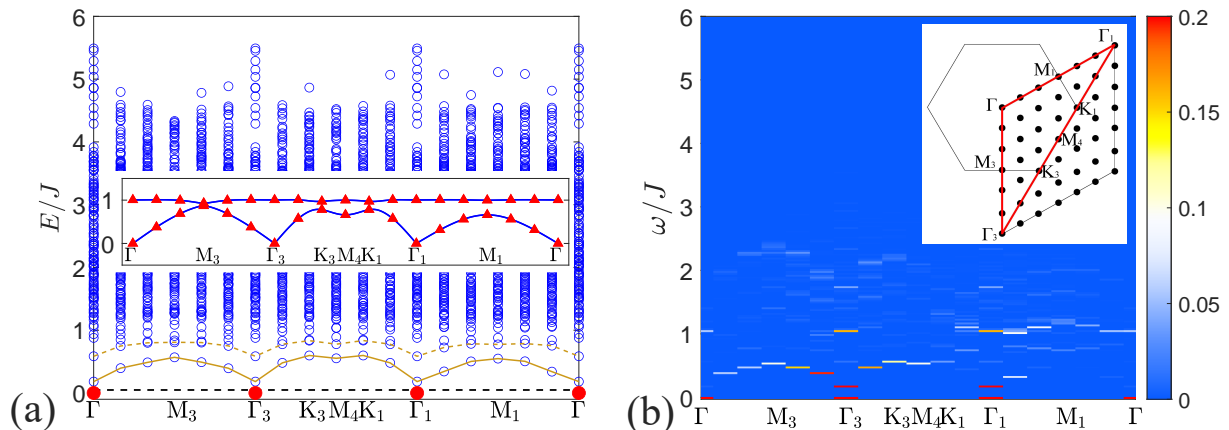


FIG. 5: (a) VMC excitation spectrum and (b) dynamic structure factor for the AFM_{ab} phase (in a system with 72 sites) with parameters $J = 1, \delta = 0.6, \Gamma' = 0, B_c = 1$. The black dashed line in (a) is the energy of the ground state before the ‘renormalization’, while the red dot stands for the ‘renormalized’ one. The inset of (a) shows the one-magnon bands from linear spin wave theory, and the inset of (b) illustrates the Brillouin zone and the path of the excitation spectrum.

netic field as in the region-I (see Fig.2(b)(I)&(IV)). In the second part, there is an intermediate stripe phase under a proper magnetic field as in the region-II (see Fig.2(b)(II)&(V)). In the last part, there is also an intermediate phase that exhibits zigzag order as in the region-III (see Fig.2(b)(III)&(VI)). The magnon excitations are also gapped in the intermediate stripe and zigzag phases. In all the above cases, the phase transition from the intermediate phase to the dimerized or polarized phase is continuous, while the transition from the intermediate phase to the low-field AFM_c phase is of first order (for details see Appendix A).

From the phase diagram, we can see that the dimerized ground state at $\mathbf{B} = 0$ is not a necessary condition for the existence of the field-induced intermediate magnetically ordered phase. Therefore, the physics of this system would be further enriched by proper spin-orbit couplings. In the next section, we will interpret the nature of the continuous transitions from the VMC approach, and then attribute the occurrence of the intermediate ordered phase to the condensation of magnons carrying nonzero momentum.

B. Field-induced Continuous Phase Transitions

1. Low-field and high-field limit

As a typical example, we mainly focus on the interaction parameter region of the dimerized phase. In the dimerized phase, the spinons are confined in the singlet ($S = 0$), three energy-degenerate triplets ($S = 1$), and high-energy continua.

The renormalized excitation spectrum for the $\mathbf{k} = 0$ are shown in Fig.4(a). Here we can clearly see the singlet and triplet states at low energies, and higher energy

continues. Because SOC disappears here, S^c along the magnetic field (c -direction) is a good quantum number, then we could divide them into three classes according to $S^c = -1, 0, 1$. When a magnetic field is added, Zeeman terms are added. In orthogonal normalization excitation space, Zeeman terms only appear in diagonals, and produce a splitting of energy without a change of state. Energy splitting lines between singlet and triplet states are plotted in Fig.4(a), they close the gap at $B_c/J \approx 0.89$, which means a continuous transition, i.e. magnon BEC.

At high-field limit, the polarized state is the ground state, $S^c = L/2$ is also a conserved quantity. The low energy excited state is in space $S^c = L/2 - 1$ with dimension L , hence we could obtain exact Hamiltonian \mathcal{H} in this space, $\mathcal{H}_{i,j} = \langle i|H|j \rangle$, where $|i(j)\rangle$ means the configuration flip $i(j)$ -th from the polarized state. Then diagonalize \mathcal{H} to get the spectrum of this excitation space, we plot the excitation energy in Fig.4(b). When the magnetic field drops to $B_c/J = 1.2$, gap close, implied this is also a continuous phase transition from AFM_{ab} to the polarized state. These results are consistent with previous studies^{13,14}, which once again demonstrate the reliability of our VMC method. If SOC appears (namely, nonzero Γ' interactions), we believe that similar results will indicate continuous phase transitions.

2. Intermediate field region

Now we study the low-energy physics of the intermediate phase and will focus on the AFM_{ab} phase as an example. We will calculate the excitation spectrum and the dynamic structure factor (DSF)⁴⁶ with interaction parameters $J = 1, \delta = 0.6, \Gamma' = 0, B_c = 1$.

The excitation spectrum and DSF for the AFM_{ab} phase are obtained from the renormalized spinons excitations as discussed in Sec.III B. For simplicity, we consider

the path in momentum points as plotted in the inset of Fig.5(b), which includes 2 different \mathbf{K} points and 3 different \mathbf{M} points. The magnons as bound states of spinons are clearly seen in Fig.5(a), which are well separated from the continuum. Especially, the lowest energy band (the orange solid line) agrees well with the lowest magnon band calculated from linear spin wave theory [see the insert of Fig.5(a)]. The small gap at the Γ point in the magnon is owing to system size effect. However, the second excitation band [the orange dashed line in Fig.5(a)] is dispersive and deviates with the dispersion of the upper magnon band (which is quite flat) in the linear spin wave theory.

Fig.5(b) shows the zz -component of the DSF which can be measured in neutron scattering experiments,

$$S^{zz}(\mathbf{q}, \omega) = \sum_n |\langle \Psi_n^{\mathbf{q}} | S_{\mathbf{q}}^z | \Psi_0 \rangle|^2 \delta(\omega - E_n^{\mathbf{q}} + E_0)$$

where $|\Psi_0\rangle$ is the variational ground state with energy E_0 and $|\Psi_n^{\mathbf{q}}\rangle$ is the n -th ‘renormalized’ two-spinon excited state with momentum \mathbf{q} and energy $E_n^{\mathbf{q}}$. We note that $S_{\mathbf{q}}^z = \frac{1}{\sqrt{L}} \sum_{\mathbf{r}} \exp[i\mathbf{q} \cdot \mathbf{r}] S_{\mathbf{r}}^z$ is the Fourier-transformed spin operator for the component z , with L being the number of sites in the system.

Comparing Fig.5(a) and Fig.5(b), it can be seen that the lower magnon band contributes a big weight in the DSF data. In contrast, the second band in the renormalized excitations, which is dispersive, has a very small weight. However, there is indeed an almost flat band in the DSF data at around $\omega/J \approx 1$, whose dispersion is qualitatively consistent with the upper magnon band in linear spin wave theory. Therefore, it is better not to identify the second excitation band (the dashed line) in Fig.5(a) as the upper magnon band, instead, the upper magnon band locates somewhere inside the continuum. If this is true, then it means that there are nonzero density of states between the lower and upper magnon bands, which is quite unusual in quantum antiferromagnets. The weight of the DSF signal for the magnon bands almost vanishes at some momentum points, the reason might be that we only considered the zz -component. Finally, the higher-energy continuum contributes small but nonzero weight to the DSF, indicating that quantum fluctuations at $\omega > J$ (above the magnon bands) is not negligible.

The DSF for the intermediate stripe and zigzag ordered phases will not be shown here.

V. CONDENSATION OF MAGNONS AND DYNAMIC CRITICAL EXPONENT

A. Higher-field Critical Points

In this section, we will adopt the Holstein-Primarkov representation⁴⁷ of spins and calculate the magnon spectrum. As illustrated above, at the critical point where the magnon gap closes, the magnons condense and the

system undergoes a continuous phase transition. If the magnon gap closes at momentum \mathbf{Q} , then after the phase transition the system exhibits a long-range magnetic order whose static structure factor supports a peak at momentum \mathbf{Q} .

We will start with the polarized state in the high field limit, where the excitations are gapped bosonic magnons. Actually, when in the $B \rightarrow \infty$ limit, the system approximately recovers the $O(2)$ symmetry (and hence the BEC picture approximately works). If the magnetic field is oriented along the c -direction, we can choose c -direction as the new axes S'^z . To this end, we perform a uniform orthogonal transformation without changing the excitation spectrum,

$$\begin{pmatrix} S'_x \\ S'_y \\ S'_z \end{pmatrix} = \begin{pmatrix} \frac{1}{\sqrt{2}} & \frac{-1}{\sqrt{2}} & 0 \\ \frac{1}{\sqrt{6}} & \frac{1}{\sqrt{6}} & \frac{-2}{\sqrt{6}} \\ \frac{1}{\sqrt{3}} & \frac{1}{\sqrt{3}} & \frac{1}{\sqrt{3}} \end{pmatrix} \begin{pmatrix} S_x \\ S_y \\ S_z \end{pmatrix}. \quad (7)$$

Thus the model (1) is transformed into a new one under the above orthogonal transformation.

To obtain the spin wave spectrum, we will adopt the Holstein-Primakoff representation⁴⁷ in the new spin frame,

$$\begin{aligned} S'_x &= \frac{1}{2} \left(a_i^\dagger \sqrt{1 - a_i^\dagger a_i} + \sqrt{1 - a_i^\dagger a_i} a_i \right) \sim \frac{1}{2} (a_i^\dagger + a_i), \\ S'_y &= \frac{i}{2} \left(a_i^\dagger \sqrt{1 - a_i^\dagger a_i} - \sqrt{1 - a_i^\dagger a_i} a_i \right) \sim \frac{i}{2} (a_i^\dagger - a_i), \\ S'_z &= \frac{1}{2} - a_i^\dagger a_i, \end{aligned} \quad (8)$$

where the bosons satisfy the usual commutation relations $[a_i, a_j^\dagger] = \delta_{ij}$. Substituting above formulas into the transformed spin-spin interactions and keeping the quadratic terms, we obtain the following Hamiltonian in the Fourier bases,

$$H_{\text{SW}} = \sum_{\mathbf{k}} \Psi^\dagger(\mathbf{k}) \mathcal{H}(\mathbf{k}) \Psi(\mathbf{k}), \quad (9)$$

where $\Psi^\dagger(\mathbf{k}) = (a_{\mathbf{k}A}^\dagger, a_{\mathbf{k}B}^\dagger, a_{-\mathbf{k}A}, a_{-\mathbf{k}B})$ with $a_{A,B}^\dagger$ ($a_{A,B}$) being the magnon creation (annihilation) operator on sublattice A (B). It is important to note that unlike the fermionic case, the eigenenergies and eigenmodes in this case are obtained by diagonalizing the non-Hermitian matrix $\Sigma \mathcal{H}(\mathbf{k})$, where $\Sigma = \text{diag}(1, 1, -1, -1)$. Thus diagonalizing the above non-Hermitian matrix, we obtain the magnon excitations spectrum.

The magnon gap decreases when lowering the field strength. At a critical field, the magnon gap closes at a certain momentum point in the Brillouin zone (see Fig.6) and the system undergoes a continuous phase transition. The momentum at which the magnon gap closes depends on the interaction parameters. If one further decreases the field strength, then the magnon spectrum in spin-wave Hamiltonian (9) will have an imaginary part, indicating that the polarized state is unstable. To avoid the

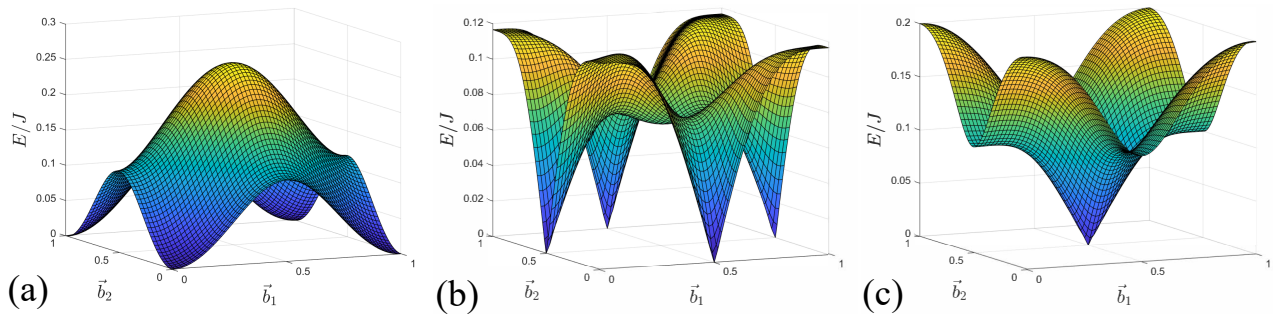


FIG. 6: Condensation of magnons (the lowest band in linear spin wave theory) at the upper critical point. (a) $\delta = 0.8, \Gamma'/J = 0.1$, the magnon gap closes at the Γ point ($\mathbf{k} = 0$) with a quadratic dispersion; (b) $\delta=0.85, \Gamma'/J=0.2$, the magnon gap closes at the \mathbf{M}_1 point ($\mathbf{k} = \mathbf{b}_1/2$ or $\mathbf{k} = \mathbf{b}_2/2$) with a linear dispersion; (c) $\delta=0.9, \Gamma'/J=0.2$, the magnon gap closes at point the \mathbf{M}_2 point ($\mathbf{k} = \mathbf{b}_1/2 + \mathbf{b}_2/2$) with a linear dispersion.

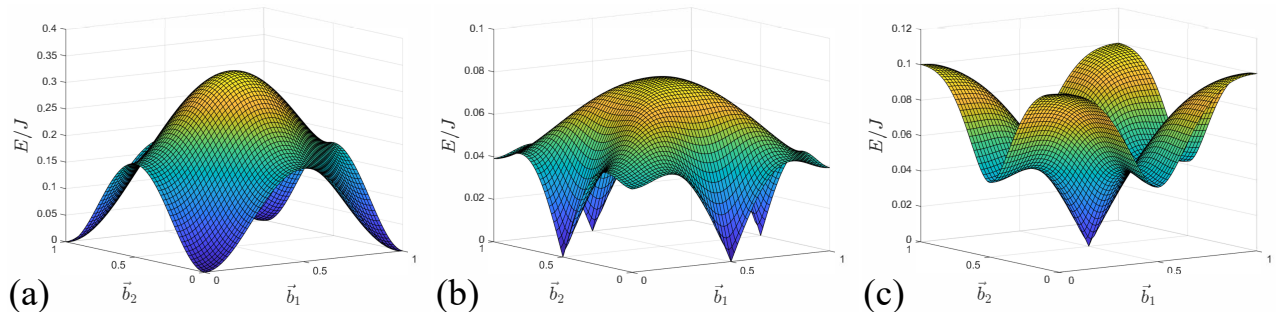


FIG. 7: Condensation of magnons (the lowest band in $SU(4)$ spin wave theory) at the lower critical point. (a) $\delta = 0.8, \Gamma'/J = 0.05$, the magnon gap closes at the Γ point with a quadratic dispersion; (b) $\delta=0.9, \Gamma'/J=0.1$, the magnon gap closes at the \mathbf{M}_1 point with a linear dispersion; (c) $\delta=0.95, \Gamma'/J=0.1$, the magnon gap closes at the \mathbf{M}_2 point with a linear dispersion.

instability in the excitation spectrum, the system enters an ordered phase where the spins exhibit a different configuration. In other words, the condensation of magnons results in a long-range magnetic order and the excitation spectrum changes accordingly.

If Γ' is small, the magnons condense at the Γ point (i.e. $\mathbf{k} = 0$) and the system exhibits canted Néel order after the phase transition. As shown in Fig.6(a), the dynamic critical exponent is $z = 2$ at the transition point (owing to the quadratic dispersion), which is the same as the conventional magnon BEC¹⁴ with $\Gamma' = 0$. On the other hand, if the magnons condense at the \mathbf{M}_1 point (i.e. $\mathbf{k} = \mathbf{b}_1/2$ or $\mathbf{k} = \mathbf{b}_2/2$), then the system transits to the stripe phase and if the magnons condense at the \mathbf{M}_2 point (i.e. $\mathbf{k} = \mathbf{b}_1/2 + \mathbf{b}_2/2$), then the system exhibits zigzag order. In these cases, the dynamical exponent is $z = 1$, as shown in Fig.6(b)&(c) where the magnon gap closes linearly. From the dynamic critical exponent, it is expected that the correlation length near the critical point is given by $\xi \sim |B_c - B_{\text{critical}}|^{-\nu}$ with $\nu = 1/z$ in two spatial dimension if the continuous $O(2)$ symmetry is present^{48,52}. Therefore, SOC is crucial to understand the nature of the field-induced quantum critical points beyond the conventional magnon BEC.

	Intermediate phase	Lower QCP	Upper QCP
$\Gamma' = 0$	AFM _{ab}	$z = 2$	$z = 2$
$\Gamma' \neq 0$	AFM _{ab}	$z = 2$	$z = 2$
	Stripe	$z = 1$	$z = 1$
	Zigzag	$z = 1$	$z = 1$

TABLE I: The dynamic critical exponent of field-induced quantum critical points (QCP) with or without Γ' interactions from spin wave theory.

B. Lower-field Critical Points

Now we go to the low field limit. When SOC is weak, the system enters the dimerized phase when the magnetic field is weak. As illustrated in the previous section, the magnon bands split into three branches (for details see Appendix A) and the gap of the lowest branch (b_+) decreases linearly with the field strength, the magnon gap closes and the system enters the intermediate ordered phase when the field strength reaches a critical point.

To obtain the critical exponent at the lower critical points, we consider each z -bond as an effective site, which contains four internal degrees of freedom. By regarding the four bases on each effective site as a ‘ $SU(4)$ spin’, namely, by mapping the four bases $|\uparrow\uparrow\rangle, |\uparrow\downarrow\rangle, |\downarrow\uparrow\rangle, |\downarrow\downarrow\rangle$ on

the dimer bond into four species of boson operators

$$B^\dagger = (b_{\uparrow\uparrow}^\dagger, b_{\uparrow\downarrow}^\dagger, b_{\downarrow\uparrow}^\dagger, b_{\downarrow\downarrow}^\dagger)$$

we can figure out the $SU(4)$ spin wave⁵⁰, where the ‘classical’ ground state is a singlet formed by the two spin-1/2 spins on each effective site

$$|\text{Dimer}\rangle = \prod_i \left[\frac{1}{\sqrt{2}} (b_{\uparrow\downarrow}^\dagger - b_{\downarrow\uparrow}^\dagger) \right]_i |\text{vac}\rangle. \quad (10)$$

By adopting the Holstein–Primakoff approximation⁵¹ and keeping the quadratic terms only, we obtain the spin-wave Hamiltonian (for details of calculations see Appendix C), which can be diagonalized using bosonic Bogoliubov transformation.

The dispersions of the b_+ branch in $SU(4)$ spin wave theory are shown in Fig.7, it can be found that the dynamic critical exponent at the lower-field critical point is the same as that in the higher-field critical point (see Fig.6 for illustration). Namely, the dynamic critical exponent is $z = 2$ for the transition from the dimerized phase to the Néel phase and is $z = 1$ for the transitions from the dimerized phase to the stripe phase or to the zigzag phase, which are summarized in Tab.I.

When Γ' interaction is large enough, the gap of b_0 branch will close, which means that the ground state will become Néel order where the spins are oriented perpendicular to the honeycomb plane through a continuous phase transition. In this case, with the increasing of field strength, the system enters field-induced in-plane ordered phases by a first-order phase transition (see Appendix A for details).

VI. CONCLUSIONS AND DISCUSSIONS

We studied the J - Γ' model on the distorted honeycomb lattice in a magnetic field via variational Monte Carlo method. We conclude that in a dimerized antiferromagnet the external magnetic field will generally induce an intermediate phase with long-range antiferromagnetic orders, no matter if the ground state at zero field is a non-magnetic state with dimerized singlets or an AFM ordered state. The ordering pattern in the intermediate phase can be interpreted from the high-field or low-field limit, where the magnon gap closes at a certain point in the Brillouin zone with decreasing or increasing of the magnetic field strength. While the phase transitions are continuous, the nature of the field-induced quantum critical points can be different from the conventional magnon Bose-Einstein condensation.

In obtaining the classical order, we have used the canted single- \mathbf{Q} approximation. We cannot rule out the possibility that the classical magnetic order is a multi- \mathbf{Q} state instead of a single- \mathbf{Q} state. Therefore, the spin-orbit coupled spin model deserves to study with different numerical approaches.

In the present work, we only considered the uniform Γ' interactions to study the effect of spin-orbit coupling in dimerized antiferromagnets. By tuning on other interactions (such as Kitaev interactions, off-diagonal symmetric interactions, and Dzyaloshinskii-Moriya interactions), the intermediate field region may contain more than one ordered phase. In that case, the experimental observations in $\text{Yb}_2\text{Si}_2\text{O}_7$ may be explained. We will leave this possibility for future work.

Acknowledgements

We are grateful to J. Ye for helpful discussions. This work is supported by the NSF of China (No. 11574392), the National Natural Science Foundation of China (No. 12134020), the Fundamental Research Funds for the Central Universities and the Research Funds of Renmin University of China (No. 19XNLG11), and the China Postdoctoral Science Foundation (No. 2021M690093).

Appendix A: Phase transitions from AFM_c to others

1. To the dimerized phase

When the magnetic field $B_c = 0$, with the increasing of Γ' interactions, the system undergoes a continuous phase transition from the dimerized phase to the AFM_c phase where the spin orientation is parallel to the c -direction (see Fig.2). The question is how to understand the physical mechanism of phase transition. In the dimerized phase, three magnons bands split from each other due to the appearance of magnetic fields. We call the middle magnon band b_0 , the lowest band b_+ , and highest band b_- , respectively (see Fig.8(a)). Meanwhile, the gap of b_0 -band is independent on the c -direction field while the gap of b_+ -band or b_- -band is dependent on the field. In other words, the gap of b_0 -band does not respond to magnetic fields, which means the b_0 -band supports an antiferromagnetic pattern in the direction of the magnetic field. Thus the mechanism behind the phase transition (between AFM_c and dimerized phase) is that the gap of b_0 -band (in $SU(4)$ spin wave theory) will close as Γ' interactions increase. This condensation is at $\mathbf{\Gamma}$ point with dynamic critical exponent $z = 1$ (see Fig.8(b)).

2. To intermediate ordered phases

When turning on the magnetic field B_c , the AFM_c state will undergo two successive phase transitions. The first transition is of first order, and the second one is of second order. The first-order phase transition is reflected by the level crossing of the energy curve of the ground state, as shown in Fig.9. It is important to note that the energy difference between ground state and other ordered states in the intermediate field region is very visible

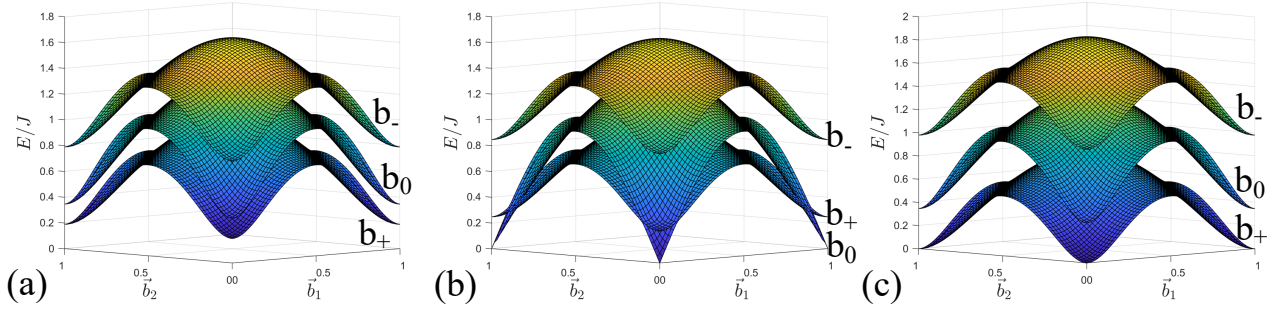


FIG. 8: The $SU(4)$ spin wave spectrum. (a) $\delta = 0.6$, $\Gamma'/J = 0.02$, $B_c/J = 0.3$. The dimerized ground state appears here and three magnon bands (namely, b_+ , b_0 , and b_- , respectively) split from each other due to nonzero magnetic fields. (b) $\delta = 0.6$, $\Gamma'/J = 0.05$, $B_c/J = 0.3$. The gap of b_0 -band closes, and the condensation of b_0 -band indicates the continuous transition from the dimerized state to AFM_c with a Néel pattern in the c -direction. (c) $\delta = 0.6$, $\Gamma'/J = 0.02$, $B_c/J = 0.49$. The gap of b_+ -band closes, and the condensation of b_+ -band indicates a continuous transition from the dimerized state to AFM_{ab} with canted axis along c -direction.

(at least $10^{-2}J$ per site) although the difference between them looks small in Fig.9.

The occurrence of the first order phase transition can also be understood from the condensation of different magnons from the ‘ $SU(4)$ spin wave’ theory (see Appendix C). To be specific, the condensation of the b_+ -band indicates (at the Γ , \mathbf{M}_1 or \mathbf{M}_2 point in the Brillouin zone) an antiferromagnetic pattern in the honeycomb plane (corresponding to AFM_{ab} , stripe or zigzag, respectively). As a typical example shown in Fig.8(c), the continuous phase transitions can be attributed to the gap-closure of the b_+ -band with the increase of field strength. On the other hand, the condensation of the b_0 -band [at the Γ point, see Fig.8(b)] represents an antiferromagnetic pattern in c -direction (corresponding to AFM_c). Generally, the AFM_c order comes from the condensation of the b_0 -band while the intermediate ordered phases (such as AFM_{ab} , stripe, or zigzag) result from the condensation of the b_+ -band. Naturally, the phase transition between AFM_c and intermediate ordered phases is first-order.

Depending on the ordering pattern of the intermediate phases (namely, the AFM_{ab} order, the stripe order or the zigzag order), the AFM_c phase splits into three regions labeled as IV, V, VI, respectively. It should be noticed that when $\Gamma' = 0$ and $\delta < 0.5$, an infinitesimally small magnetic field can tilt the direction of the magnetic momentum such that the system exhibits in-plane AFM order.

Appendix B: Spin wave spectrum at high fields

To study the condensation of bosons from the polarized state, we adopt the linear spin wave theory. Firstly,

constructing rotation matrix \mathcal{R} :

$$\mathbf{S}' = \begin{pmatrix} S'^x \\ S'^y \\ S'^z \end{pmatrix} = \mathcal{R}\mathbf{S} = \begin{pmatrix} \frac{1}{\sqrt{2}} & \frac{-1}{\sqrt{2}} & 0 \\ \frac{1}{\sqrt{6}} & \frac{1}{\sqrt{6}} & \frac{-2}{\sqrt{6}} \\ \frac{1}{\sqrt{3}} & \frac{1}{\sqrt{3}} & \frac{1}{\sqrt{3}} \end{pmatrix} \begin{pmatrix} S^x \\ S^y \\ S^z \end{pmatrix} \quad (\text{B1})$$

hence the S'^z is along the original c -direction.

Secondly, we rewrite model (1):

$$\begin{aligned} H &= \sum_{\langle i,j \rangle \in \gamma} \mathbf{S}_i^\dagger \mathcal{H}_\gamma \mathbf{S}_j - \sum_i \mathbf{B} \cdot \mathbf{S}_i \\ &= \sum_{\langle i,j \rangle \in \gamma} \mathbf{S}_i^\dagger \mathcal{R}^\dagger \mathcal{R} \mathcal{H}_\gamma \mathcal{R} \mathcal{R}^\dagger \mathbf{S}_j - \sum_i \mathbf{B} \mathcal{R}^\dagger \cdot \mathcal{R} \mathbf{S}_i \\ &= \sum_{\langle i,j \rangle \in \gamma} \mathbf{S}_i'^\dagger \mathcal{H}'_\gamma \mathbf{S}_j' - \sum_i \mathbf{B}' \cdot \mathbf{S}_i' \end{aligned} \quad (\text{B2})$$

and \mathbf{B}' is in the same direction with S'^z .

We will obtain an effective bosonic model through rewriting model (B2) by Holstein-Primakoff transformation

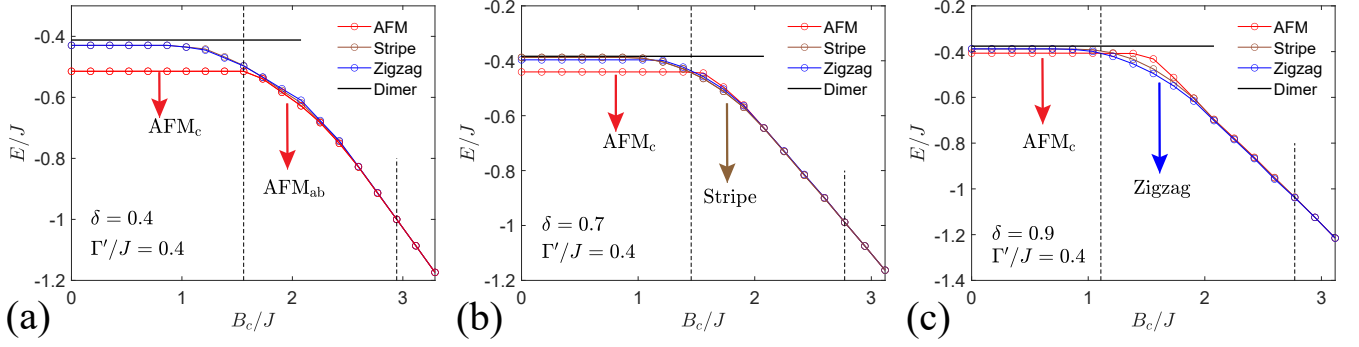


FIG. 9: Energy curves of the ground state with the increasing magnetic field (in the parameter region of AFM_c at zero field). (a) $\delta=0.4$, $\Gamma'/J=0.4$, (b) $\delta=0.7$, $\Gamma'/J=0.4$, (c) $\delta=0.9$, $\Gamma'/J=0.4$ are points in region-IV, region-V, and region-VI with triangle (see Fig.2) respectively. The vertical dashed lines indicate the values of the critical fields.

(8). Then spin interaction terms become

$$\begin{aligned}
S_i^x S_j^x &= \frac{1}{4}(a_i^\dagger a_j^\dagger + a_i^\dagger a_j + a_i a_j^\dagger + a_i a_j), \\
S_i^y S_j^y &= \frac{1}{4}(-a_i^\dagger a_j^\dagger + a_i^\dagger a_j + a_i a_j^\dagger - a_i a_j), \\
S_i^z S_j^z &= a_i^\dagger a_i a_j^\dagger a_j - \frac{1}{2}(a_i^\dagger a_i + a_j^\dagger a_j) + \frac{1}{4}, \\
S_i^x S_j^y &= \frac{i}{4}(a_i^\dagger a_j^\dagger - a_i^\dagger a_j + a_i a_j^\dagger - a_i a_j), \\
S_i^y S_j^x &= \frac{i}{4}(a_i^\dagger a_j^\dagger + a_i^\dagger a_j - a_i a_j^\dagger - a_i a_j), \\
S_i^x S_j^z &= -\frac{1}{2}(a_i^\dagger a_j^\dagger a_j + a_i a_j^\dagger a_j) + \frac{1}{4}(a_i^\dagger + a_i), \\
S_i^z S_j^x &= -\frac{1}{2}(a_i^\dagger a_i a_j^\dagger + a_i^\dagger a_i a_j) + \frac{1}{4}(a_j^\dagger + a_j), \\
S_i^y S_j^z &= -\frac{i}{2}(a_i^\dagger a_j^\dagger a_j - a_i a_j^\dagger a_j) + \frac{i}{4}(a_i^\dagger - a_i), \\
S_i^z S_j^y &= -\frac{i}{2}(a_i^\dagger a_i a_j^\dagger - a_i^\dagger a_i a_j) + \frac{i}{4}(a_j^\dagger - a_j), \\
B^z S_i^z &= B^z (\frac{1}{2} - a_i^\dagger a_i). \tag{B3}
\end{aligned}$$

Only keeping the quadratic term, we can obtain spin-wave Hamiltonian (9) by Fourier transformation. Because of continuous phase transitions, we tune the chemical potential term $\sum_i \lambda a_i^\dagger a_i$ to make the magnon dispersion touch to the zero energy. The momentum at a gapless point is carried by a specific in-plane magnetic order. If $\delta \neq 0$, C_3 symmetry is broken. The inequivalent \mathbf{M} points mean stripe orders and zigzag orders, respectively. Therefore we can distinguish the condensate momentum of AFM, stripe, and zigzag orders. As shown in Fig.6, they condense at Γ , \mathbf{M}_1 , and \mathbf{M}_2 , respectively.

Appendix C: $SU(4)$ spin wave spectrum at low fields

In the low field region, the ground state for small Γ' is a singlet state composed of the direct product of singlet dimers. Noticing that each dimer contains two spins $S =$

$\frac{1}{2}$ which span a 4-dimensional Hilbert space, so we regard each dimer as an effective site placed with a $SU(4)$ spin. In the following, we construct the $SU(4)$ spin wave theory on the square lattice formed by the effective sites.

Firstly, we introduce four species of boson operators

$$B^\dagger = (b_{\uparrow\uparrow}^\dagger, b_{\uparrow\downarrow}^\dagger, b_{\downarrow\uparrow}^\dagger, b_{\downarrow\downarrow}^\dagger)$$

to represent the four bases $|\uparrow\uparrow\rangle, |\uparrow\downarrow\rangle, |\downarrow\uparrow\rangle, |\downarrow\downarrow\rangle$ on the dimer bond respectively. Here we have omitted the site indices. This is the generalized Schwinger representation of spins and the mapping is exact if the particle number constraint $B^\dagger B = 1$ is satisfied on each bond.

The spin operators on the A sublattice are represented by

$$S_A^m = B^\dagger \frac{\sigma^m}{2} \otimes \sigma^0 B$$

with σ^0 the 2×2 identity matrix, and the spin operators on the B sublattice are represented by

$$S_B^m = B^\dagger \sigma^0 \otimes \frac{\sigma^m}{2} B.$$

It is more convenient to combine these boson operators into the eigen modes $b_{S,m}$ with the total spin quantum number S (for the two spins on the dimer bond) and its eigenvalue m of the S^z -component, namely,

$$\begin{aligned}
\tilde{B}^\dagger &= (b_{0,0}^\dagger, b_{1,1}^\dagger, b_{1,0}^\dagger, b_{1,-1}^\dagger) = (b_{\uparrow\uparrow}^\dagger, b_{\uparrow\downarrow}^\dagger, b_{\downarrow\uparrow}^\dagger, b_{\downarrow\downarrow}^\dagger) U \\
\text{with } U &= \begin{pmatrix} 0 & 1 & 0 & 0 \\ \frac{\sqrt{2}}{2} & 0 & \frac{\sqrt{2}}{2} & 0 \\ -\frac{\sqrt{2}}{2} & 0 & \frac{\sqrt{2}}{2} & 0 \\ 0 & 0 & 0 & 1 \end{pmatrix}. \text{ The advantage of adopting}
\end{aligned}$$

these new bases is that when the Heisenberg interactions on the strong bonds are dominating, we can approximately regard the ground state as the product of singlets on the strong bonds,

$$|\text{Dimer}\rangle = \prod_i (b_{0,0}^\dagger)_i |\text{vac}\rangle, \tag{C1}$$

here $|\text{vac}\rangle$ stands for the vacuum state and i labels the new site index.

In the new bases, the spin operators are rewritten as

$$S_A^m = \tilde{B}^\dagger U^\dagger \frac{\sigma^m}{2} \otimes \sigma^0 U \tilde{B}$$

for the A-sublattice and

$$S_B^m = \tilde{B}^\dagger U^\dagger \sigma^0 \otimes \frac{\sigma^m}{2} U \tilde{B}$$

for the B-sublattice.

Then we can rewrite the spin-spin interactions in forms of the boson operators \tilde{B} . For instance, on a strong bond (namely the z -bond), the Heisenberg interaction $\mathbf{S}^A \cdot \mathbf{S}^B$ is represented as

$$\mathbf{S}^A \cdot \mathbf{S}^B = -\frac{3}{4} b_{0,0}^\dagger b_{0,0} + \frac{1}{4} \sum_m b_{1,m}^\dagger b_{1,m}.$$

Secondly, we will adopt the Holstein-Primakoff approximation⁵¹ using dimerized singlets (C1) as the ground state, namely,

$$b_{0,0}^\dagger, b_{0,0} = \sqrt{1 - \sum_{m=1}^3 b_{1,m}^\dagger b_{1,m}} \approx 1.$$

Only keeping the quadratic term according to the boson operators, we obtain a quadratic Hamiltonian for the bosons.

Thirdly, performing Fourier transformation, $b_{\mathbf{k},s,m}^\dagger = \frac{1}{\sqrt{L}} \sum_{\mathbf{r}} b_{\mathbf{r},s,m}^\dagger \exp[i\mathbf{k} \cdot \mathbf{r}]$, we could obtain quadratic form Hamiltonian in momentum space,

$$H_{\text{SW}} = \sum_{\mathbf{k}} \Psi^\dagger(\mathbf{k}) \mathcal{H}(\mathbf{k}) \Psi(\mathbf{k}), \quad (\text{C2})$$

with $\Psi^\dagger(\mathbf{k}) = (b_{1,1}^\dagger(\mathbf{k}), b_{1,0}^\dagger(\mathbf{k}), b_{1,-1}^\dagger(\mathbf{k}), b_{1,1}(-\mathbf{k}), b_{1,0}(-\mathbf{k}), b_{1,-1}(-\mathbf{k}))$, and $\mathcal{H}(\mathbf{k})$ is the 6 by 6 matrix.

Finally, we could obtain magnon dispersions in Fig.7 by diagonalizing the non-Hermitian matrix $\Sigma \mathcal{H}(\mathbf{k})$, where $\Sigma = \text{diag}(1, 1, 1, -1, -1, -1)$.

* Electronic address: liuxzphys@ruc.edu.cn

† Electronic address: wangjiucui@mail.tsinghua.edu.cn

¹ T. Giamarchi and A. M. Tsvelik, *Phys. Rev. B* **59**, 11398 (1999).

² T. Matsubara and H. Matsuda, *Progress of Theoretical Physics* **16**, 569 (1956).

³ C. Rüegg, N. Cavadini, A. Furrer, H.-U. Güdel, K. Krämer, H. Mutka, A. Wildes, K. Habicht, and P. Vorderwisch, *Nature (London)* **423**, 62 (2003).

⁴ S. O. Demokritov, V. E. Demidov, O. Dzyapko, G. A. Melkov, A. A. Serga, B. Hillebrands, and A. N. Slavin, *Nature (London)* **443**, 430 (2006).

⁵ E. Y. Sherman, P. Lemmens, B. Busse, A. Oosawa, and H. Tanaka, *Phys. Rev. Lett.* **91**, 057201 (2003).

⁶ A. K. Kolezhuk, V. N. Glazkov, H. Tanaka, and A. Oosawa, *Phys. Rev. B* **70**, 020403 (2004).

⁷ C. Rüegg, D. F. McMorrow, B. Normand, H. M. Rønnow, S. E. Sebastian, I. R. Fisher, C. D. Batista, S. N. Gvasaliya, C. Niedermayer, and J. Stahn, *Phys. Rev. Lett.* **98**, 017202 (2007).

⁸ O. Rösch and M. Vojta, *Phys. Rev. B* **76**, 224408 (2007).

⁹ S. Krämer, R. Stern, M. Horvatić, C. Berthier, T. Kimura, and I. R. Fisher, *Phys. Rev. B* **76**, 100406 (2007).

¹⁰ S. Autti, Y. M. Bunkov, V. B. Eltsov, P. J. Heikkinen, J. J. Hosio, P. Hunger, M. Krusius, and G. E. Volovik, *Phys. Rev. Lett.* **108**, 145303 (2012).

¹¹ F. Fang, R. Olf, S. Wu, H. Kadau, and D. M. Stamper-Kurn, *Phys. Rev. Lett.* **116**, 095301 (2016).

¹² D. A. Bozhko, A. A. Serga, P. Clausen, V. I. Vasyuchka, F. Heussner, G. A. Melkov, A. Pomyalov, V. S. L'vov, and B. Hillebrands, *Nature Physics* **12**, 1057–1062 (2016).

¹³ T. Giamarchi, C. Rüegg, and O. Tchernyshyov, *Nature Physics* **4**, 198 (2008).

¹⁴ V. Zapf, M. Jaime, and C. D. Batista, *Reviews of Modern Physics* **86**, 563 (2014).

¹⁵ J. Sirker, A. Weiße, and O. Sushkov, *EPL (Europhysics Letters)* **68**, 275 (2004).

¹⁶ G. Hester, H. S. Nair, T. Reeder, D. R. Yahne, T. N. DeLazzer, L. Berges, D. Ziat, J. R. Neilson, A. A. Aczel, G. Sala, J. A. Quilliam, and K. A. Ross, *Phys. Rev. Lett.* **123**, 027201 (2019).

¹⁷ M. O. Flynn, T. E. Baker, S. Jindal, and R. R. P. Singh, *Phys. Rev. Lett.* **126**, 067201 (2021).

¹⁸ T. Radu, H. Wilhelm, V. Yushankhai, D. Kovrizhin, R. Coldea, Z. Tylczynski, T. Lühmann, and F. Steglich, *Phys. Rev. Lett.* **96**, 189704 (2006).

¹⁹ C. D. Batista, J. Schmalian, N. Kawashima, P. Sengupta, S. E. Sebastian, N. Harrison, M. Jaime, and I. R. Fisher, *Phys. Rev. Lett.* **98**, 257201 (2007).

²⁰ J. Schmalian and C. D. Batista, *Phys. Rev. B* **77**, 094406 (2008).

²¹ F. Sun and J. Ye, [arXiv:2011.11287 \[cond-mat.str-el\]](https://arxiv.org/abs/2011.11287).

²² F. Sun, J. Ye, and W.-M. Liu, *Phys. Rev. B* **94**, 024409 (2016).

²³ Y. Singh and P. Gegenwart, *Phys. Rev. B* **82**, 064412 (2010).

²⁴ K. W. Plumb, J. P. Clancy, L. J. Sandilands, V. V. Shankar, Y. F. Hu, K. S. Burch, H.-Y. Kee, and Y.-J. Kim, *Phys. Rev. B* **90**, 041112(R) (2014).

²⁵ W. Yao and Y. Li, *Phys. Rev. B* **101**, 086120 (2020).

²⁶ J. Ji, M. Sun, Y. Cai, Y. Wang, Y. Sun, W. Ren, Z. Zhang, F. Jin, and Q. Zhang, *Chin. Phys. Lett.* **38**(4), 047502

- (2021).
- ²⁷ X. Zhang, Y. Xu, R. Zhong, R. J. Cava, N. Drichko, and N. P. Armitage, [arXiv:2106.13418 \[cond-mat.str-el\]](#) .
- ²⁸ A. Kitaev, *Annals of Physics* **321**, 2 (2006).
- ²⁹ G. Jackeli and G. Khaliullin, *Phys. Rev. Lett.* **102**, 017205 (2009).
- ³⁰ J. Chaloupka, G. Jackeli, and G. Khaliullin, *Phys. Rev. Lett.* **105**, 027204 (2010).
- ³¹ L. Janssen, E. C. Andrade, and M. Vojta, *Phys. Rev. B* **96**, 064430 (2017).
- ³² J. Cookmeyer and J. E. Moore, *Phys. Rev. B* **98**, 060412(R) (2018).
- ³³ J. G. Rau and H.-Y. Kee, [arXiv:1408.4811 \[cond-mat.str-el\]](#) .
- ³⁴ S. M. Winter, Y. Li, H. O. Jeschke, and R. Valentí, *Phys. Rev. B* **93**, 214431 (2016).
- ³⁵ J. Chaloupka and G. Khaliullin, *Phys. Rev. B* **94**, 064435 (2016).
- ³⁶ J. Chaloupka and G. Khaliullin, *Phys. Rev. B* **92**, 024413 (2015).
- ³⁷ J. Wang, B. Normand, and Z.-X. Liu, *Phys. Rev. Lett.* **123**, 197201 (2019).
- ³⁸ J. Wang and Z.-X. Liu, *Phys. Rev. B* **102**, 094416 (2020).
- ³⁹ I. Affleck, Z. Zou, T. Hsu, and P. W. Anderson, *Phys. Rev. B* **38**, 745 (1988).
- ⁴⁰ J. Wang, Q. Zhao, X. Wang, and Z.-X. Liu, *Phys. Rev. B* **102**, 144427 (2020).
- ⁴¹ J. G. Rau, E. K.-H. Lee, and H.-Y. Kee, *Phys. Rev. Lett.* **112**, 077204 (2014).
- ⁴² T. Li and F. Yang, *Phys. Rev. B* **81**, 214509 (2010).
- ⁴³ F. Yang and T. Li, *Phys. Rev. B* **83**, 064524 (2011).
- ⁴⁴ B. D. Piazza, M. Mourigal, N. B. Christensen, G. J. Nilsen, P. Tregenna-Piggott, T. G. Perring, M. Enderle, D. F. McMorrow, D. A. Ivanov, and H. M. Rønnow, *Nature Physics* **11**, 62 (2015).
- ⁴⁵ Q.-R. Zhao and Z.-X. Liu, [arXiv:2105.08413 \[cond-mat.str-el\]](#) .
- ⁴⁶ F. Ferrari and F. Becca, *Phys. Rev. X* **9**, 031026 (2019).
- ⁴⁷ T. Holstein and H. Primakoff, *Phys. Rev.* **58**, 1098 (1940).
- ⁴⁸ S. Sachdev, *Zeitschrift für Physik B Condensed Matter* **94**, 469 (1994).
- ⁴⁹ To the best of our knowledge, the value of correlation length critical exponent ν is unknown if the continuous $O(2)$ symmetry is absent.
- ⁵⁰ Z.-Y. Dong, W. Wang, and J.-X. Li, *Phys. Rev. B* **97**, 205106 (2018).
- ⁵¹ R. A. Muniz, Y. Kato, and C. D. Batista, *Progress of Theoretical and Experimental Physics* **2014**, 803101 (2014).
- ⁵² To the best of our knowledge, the value of correlation length critical exponent ν is unknown if the continuous $O(2)$ symmetry is absent.